PROCEEDINGS A

royalsocietypublishing.org/journal/rspa

Research

Cite this article: Liu K, Novelino LS, Gardoni P, Paulino GH. 2020 Big influence of small random imperfections in origami-based metamaterials. *Proc. R. Soc. A* **476**: 20200236. http://dx.doi.org/10.1098/rspa.2020.0236

Received: 3 April 2020
Accepted: 12 June 2020

Subject Areas:
civil engineering, mechanical engineering

Keywords:
mechanical metamaterials, origami, imperfections, origami-based metamaterial

Author for correspondence:
Glaucio H. Paulino
e-mail: paulino@gatech.edu

†These authors contributed equally to this study.

Electronic supplementary material is available online at https://doi.org/10.6084/m9.figshare.c.5104003.

THE ROYAL SOCIETY PUBLISHING

Big influence of small random imperfections in origami-based metamaterials

Ke Liu[1,†], Larissa S. Novelino[2,†], Paolo Gardoni[3] and Glaucio H. Paulino[2]

[1]Division of Engineering and Applied Science, California Institute of Technology, 1200 E California Blvd, Pasadena, CA 91125, USA
[2]School of Civil and Environmental Engineering, Georgia Institute of Technology, 790 Atlantic Drive, Atlanta, GA 30332, USA
[3]Department of Civil and Environmental Engineering, University of Illinois at Urbana-Champaign, 205 North Mathews Avenue, Urbana, IL 61801, USA

GHP, 0000-0002-3493-6857

Origami structures demonstrate great theoretical potential for creating metamaterials with exotic properties. However, there is a lack of understanding of how imperfections influence the mechanical behaviour of origami-based metamaterials, which, in practice, are inevitable. For conventional materials, imperfection plays a profound role in shaping their behaviour. Thus, this paper investigates the influence of small random geometric imperfections on the nonlinear compressive response of the representative Miura-ori, which serves as the basic pattern for many metamaterial designs. Experiments and numerical simulations are used to demonstrate quantitatively how geometric imperfections hinder the foldability of the Miura-ori, but on the other hand, increase its compressive stiffness. This leads to the discovery that the residual of an origami foldability constraint, given by the Kawasaki theorem, correlates with the increase of stiffness of imperfect origami-based metamaterials. This observation might be generalizable to other flat-foldable patterns, in which we address deviations from the zero residual of the perfect pattern; and to non-flat-foldable patterns, in which we would address deviations from a finite residual.

1. Introduction and motivation

Mechanical metamaterials exhibit unconventional behaviour that is rarely found in natural materials

[1–4]. Their exclusive properties and functionalities arise from carefully architected microscopic structures, for which origami is a rich source of inspiration [5–26]. Origami-based metamaterials are able to produce negative Poisson's ratio [6–11], acoustic bandgaps [12], multi-stability [13–16,27], programmable thermal expansion [22] and tunable chirality [23]. *However, regarding practical applications of origami-based metamaterials, a few fundamental questions are yet to be answered: how robust are their special properties, and how these properties may change in the presence of imperfections?* [28–30]. In this paper, we focus on a well-known origami pattern, the Miura-ori, which, together with its variants, is perhaps the most adopted pattern for origami-based metamaterial designs [7–14,17–24]. The special properties of the Miura-ori are mainly programmed in its geometry [7,8]. Consequently, irregularities in the geometry of a Miura-ori can significantly change its mechanical behaviour [21,31,32]. For instance, the so-called 'pop-through defect' in Miura-ori, as a deterministic, localized interruption of periodic folding, was shown to affect their stiffness, towards either stiffening or softening [18]. However, in practice, small random geometric imperfections are perhaps the more likely cause of irregularity in the Miura-ori geometry. An example of this is reported in Baranger *et al*. [28], who showed that local inaccurate crease pattern greatly reduces the global out-of-plane response of an origami-like folded core. Additionally, Jianguo *et al*. [29] found that the influence of the imperfections, modelled by the buckling modes from eigenvalue analysis, strongly affect the folding behaviour of the Kresling tubular origami structure that shifts the folding sequence. Therefore, in this paper, we conduct both experiments and numerical simulations to study the statistical influence of small random geometric imperfections on the mechanical properties of Miura-ori. The type of imperfection that we are considering is fundamentally different from deterministic variations (or intentional imperfection) of origami geometry that has been studied in the literature [14,18,24,31]. *In this research, our main interest is to understand how the presence of random imperfections may hinder or enhance the functionality of origami-based metamaterials, but not to modify the mechanical properties of origami metamaterials by introducing imperfections*.

Geometric imperfections are ubiquitous due to various sources, such as misaligned crease pattern, non-uniform temperature or deterioration during service. To motivate our study, let us fold three Miura-ori with different degrees of random imperfection in the crease patterns. The imperfections are imposed by random perturbations of the nodes on the planar crease pattern to create misalignment. Since the perturbations are small, the three Miura-ori do not show any notable difference initially. However, if we try to fold them by compression simultaneously, their responses deviate significantly, as shown in figure 1*a*. This example shows that, small random geometric imperfections seem to hinder the foldability of Miura-ori, but on the other hand, increase their stiffness, which is different from geometric imperfections in lattice and thin-walled cellular materials [1,33–35].

2. Geometry and stiffness of standard Miura-ori

A standard Miura-ori unit cell is composed of identical parallelogram panels, defined by panel edge lengths a, b and sector angle α, as shown in figure 1*b*. At each vertex of this pattern, the sum of opposite sector angles equals to π, satisfying a necessary condition for flat-foldability (aka the Kawasaki theorem) as demonstrated in figure 1*c*. As a result, the Miura-ori admits a single degree-of-freedom (d.f.) rigid folding mechanism, which can be parametrized by one of the two dihedral angles β and θ. The two angles are related by $\sin^2(\beta/2) = \sin^2(\theta/2)[\cos^2\alpha + \sin^2\alpha\sin^2(\beta/2)]$ [7,8]. Ideally, when subject to compression, a Miura-ori should deform only at the folding creases, which is known as rigid origami behaviour. As the functionality of origami-based metamaterials mainly arise from large folding deformations [5–26], here we focus on the nonlinear response of imperfect origami under compressive folding. Assuming a simple discretized model (figure 1*b*) to represent the Miura-Ori unit cell and considering rigid origami behaviour, which means that there is no bending deformation and stretching deformation, the reaction force along the the x-direction

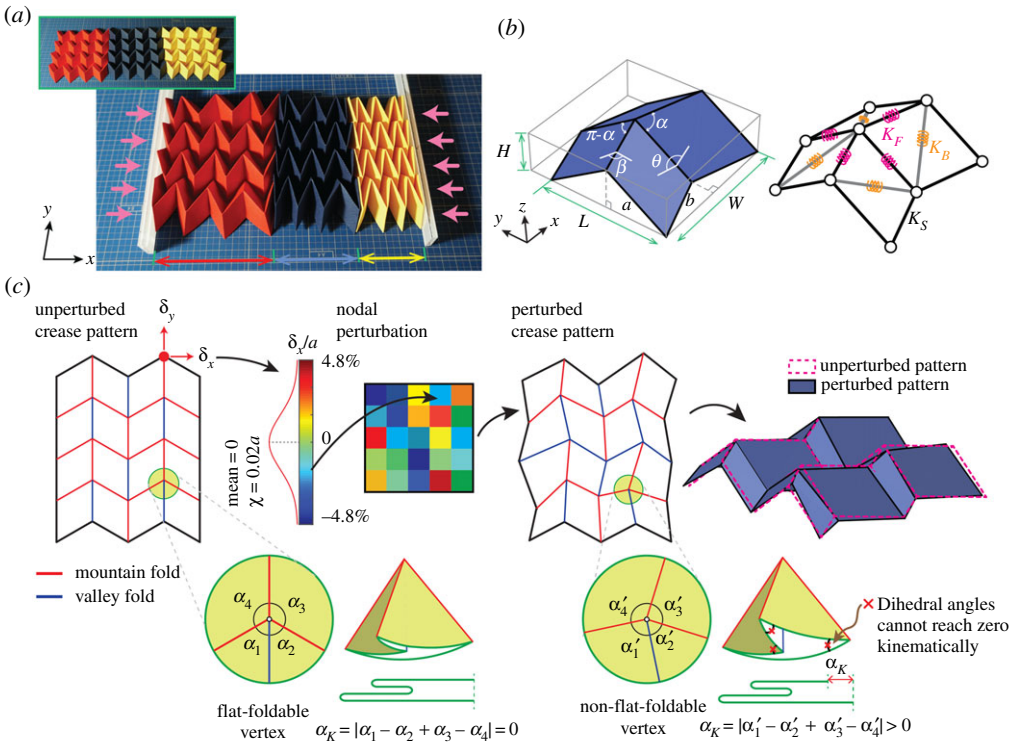

Figure 1. Geometric imperfections in origami metamaterials. (*a*) Three origami sheets under the same load. We fold the yellow one with the perfectly aligned Miura pattern. The blue one is folded from a slightly misaligned Miura pattern, and the red one is folded from a pattern with relatively strong misalignment. The inset on the upright corner shows the initial configurations of the three samples. (*b*) Geometry of the Miura-ori unit cell. The right part of (*b*) shows the schematic of a bar-and-hinge model as a simplified discretization of the Miura-ori, which we use later for the numerical simulations in this work. We discretize each quadrilateral panel into two triangles by its shorter diagonal. The parameters K_B, K_F and K_S are bending, folding and stretching stiffness, respectively. (*c*) Introduction of geometric imperfections by random nodal perturbations. At each node, the perturbation is decomposed into *x*- and *y*-directions (denoted as δ_x and δ_y). Folding up a perturbed crease patterns results in an imperfect Miura-ori, whose geometry slightly deviates from the perfect Miura-ori as indicated by magenta dashed lines. For each vertex, we compute the Kawasaki excess α_K. When $\alpha_K = 0$, the vertex is flat-foldable, which is the case for all the vertex in a standard Miura-ori pattern. However, nodal perturbation leads to $\alpha_K > 0$, in which early contact between two panels prevents the whole origami to be flattened, and some dihedral angles (marked by red crosses) cannot reach zero kinematically. (Online version in colour.)

of a Miura-ori unit cell is derived as [8]

$$F_x = 2K_F \frac{a(\theta - \theta_0)\cos^2\xi + b(\beta - \beta_0)\cos\alpha}{b\cos^2\xi \sin\alpha \cos(\theta/2)}, \tag{2.1}$$

where K_F is the assigned rotational stiffness of the hinges, $\xi = \sin^{-1}[\sin\alpha \sin(\theta/2)]$, β_0 and θ_0 define the initial partially folded configuration, and a, b are the edge length of panels.

3. Experimental analyses

All experimental samples have 4×4 unit cells, with standard geometry defined by $a = b = 25$ mm and $\alpha = 60°$. To quantitatively examine the effect of geometric imperfections, we fabricate and perform compression tests on Miura-ori samples with different degrees of random geometric imperfection. As sketched in figure 1*c*, at each node of the crease pattern, the perturbations along the *x*- and *y*-directions are sampled independently from a Gaussian distribution with

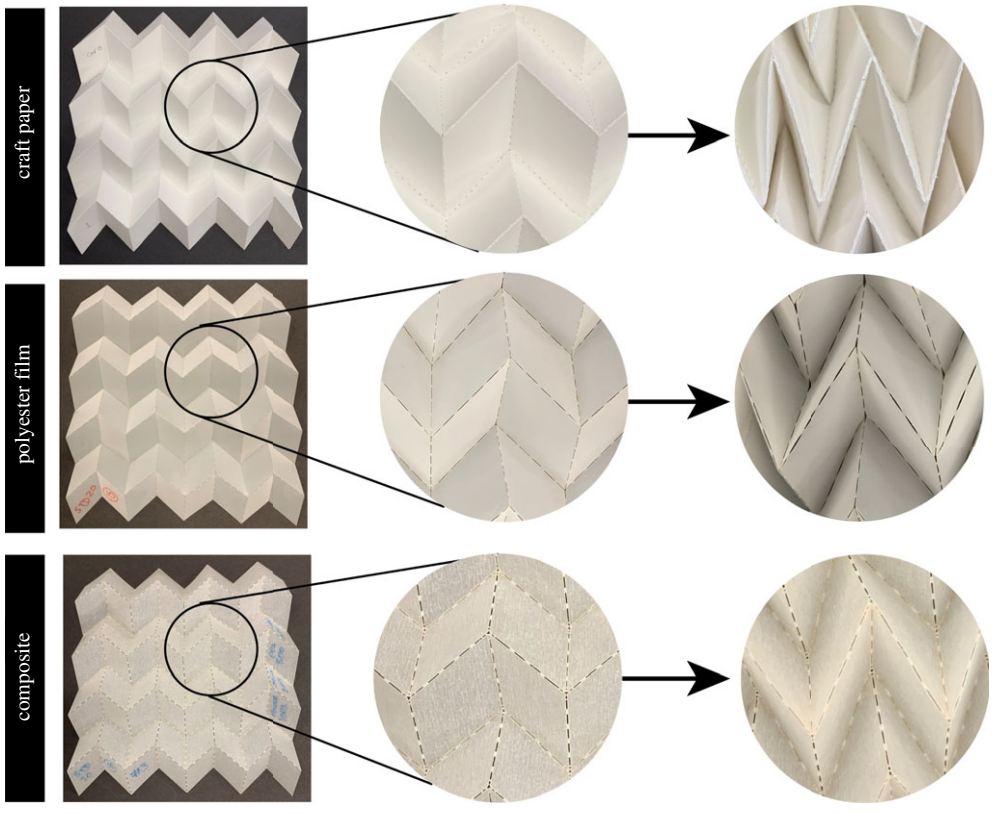

Figure 2. Zoom-in view of the creases of Miura-ori samples made from craft paper (Mi- Teintes, Canson), polyester film (Grafix Drafting Film) and composite (Durilla Durable Premium Ice Card Stock). The right-most column shows the deformation of the creases under compressive folding. We can see that the small gaps between creases being pulled open, especially for the polyester film samples.

zero mean and standard deviation χ, i.e. $N(0, \chi)$. From such sampling, we make sure that the nodal perturbations are unbiased in direction. Two representative values of χ are used to prepare two groups of perturbed patterns: $\chi = 0.01a$ and $\chi = 0.02a$. The physical samples are fabricated using three different materials: (1) craft paper (160 g m^{-2} Mi-Teintes, Canson, Young's modulus $E_S = 1219$ MPa, thickness of 0.24 mm), (2) polyester film (Grafix Drafting Film, $E_S = 2449$ MPa, thickness of 0.127 mm), and (3) composite sheet (260 g m^{-2} Durilla Durable Premium Ice Card Stock, $E_S = 1303$ MPa, thickness of 0.30 mm), as shown in figure 2. The composite sheet is made of three layers in a 'paper-film-paper' construction.

(a) Material characterization

We need to characterize the mechanical properties of the sheet materials that we are going to use. First, we describe the custom-built mechanical testing device that was developed for this study. Then we explain the basic tests that are conducted: (a) folding/bending stiffness tests; (b) compression tests; and (c) standard tensile tests. The first and second set of tests are performed on the custom-built mechanical testing device.

(i) Mechanical testing device

A custom-built mechanical testing bed, as shown in figure 3*a*,*b*, is used to measure the mechanical properties of origami metamaterials. The mechanical testing bed consists of two main parts: (1) A testing frame consists of a polished steel bed, two vertical steel plates, two guiding rails, a 50

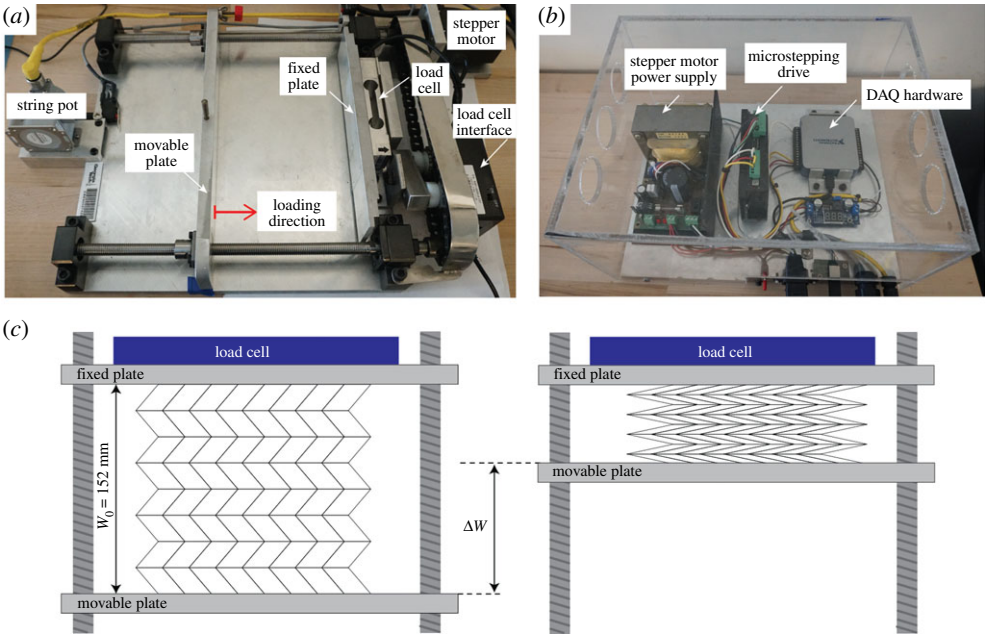

Figure 3. The mechanical testing bed for compression test of origami samples. (*a*) Testing frame. (*b*) Hardware components. (*c*) Schematics of the compression test. (Online version in colour.)

N load cell with accuracy at 0.015% of its full scale (RSP1, Loadstar Sensors), an I/O module (DI-1000 U, Loadstar Sensors) and a stepper motor (STP-MTR-23079, SureStep). (2) A control module that integrates the microstepping drive (STP-DRV-6575, SureStep), the stepper motor power supply (STP-MTR-23079, SureStep), and the data acquisition device (DAQ) (National Instruments). A LabVIEW program is used to control the system and acquire data. The procedure of the compression test of Miura-ori samples is illustrated in figure 3*c*.

(ii) Folding and bending stiffness

Bending and folding stiffness of the sheet materials are important properties when dealing with origami metamaterials. To characterize the bending stiffness of the origami panels (denoted as K_B), for each material, we prototype five rectangular panels (50 mm × 25 mm) with folded flanges that resemble the presence of neighbouring panels in an origami structure, as shown in figure 4*a*. The presence of the flanges leads to localized bending curvatures, similar to deformed origami panels [9]. In a similar manner, we also prototype five samples per material to characterize the folding stiffness of the paper creases (K_F). Each sample has two square panels of dimension 25 mm × 25 mm, jointed by a perforated crease line (figure 4*d*). The crease lines are first folded completely and then released to a neutral angle prior to the test.

The samples are tested in an adapted set-up using our custom-built mechanical testing device, as shown in figure 4. First, we attach a spacer to the movable plate. This spacer holds the sample, while leaving clearance for the free end of the sample to displace freely in space to some extent. Second, we mount a three-dimensional printed force arm to the fixed plate with its centre offset 29 mm from the spacer edge. This arm transmits the reaction force from the sample to the load cell. Figure 4*b*,*e* shows the initial set-up of the tests to measure bending stiffness and folding stiffness, respectively. Figure 4*c*,*f* sketches intermediary scenarios during the test.

The moment (M) at the crease/bending lines and the rotational angle (ψ) are calculated by

$$M = Fd_x, \psi = \tan^{-1}\left(\frac{u_0}{d_x}\right) - \tan^{-1}\left(\frac{u_0 - \Delta u}{d_x}\right), \tag{3.1}$$

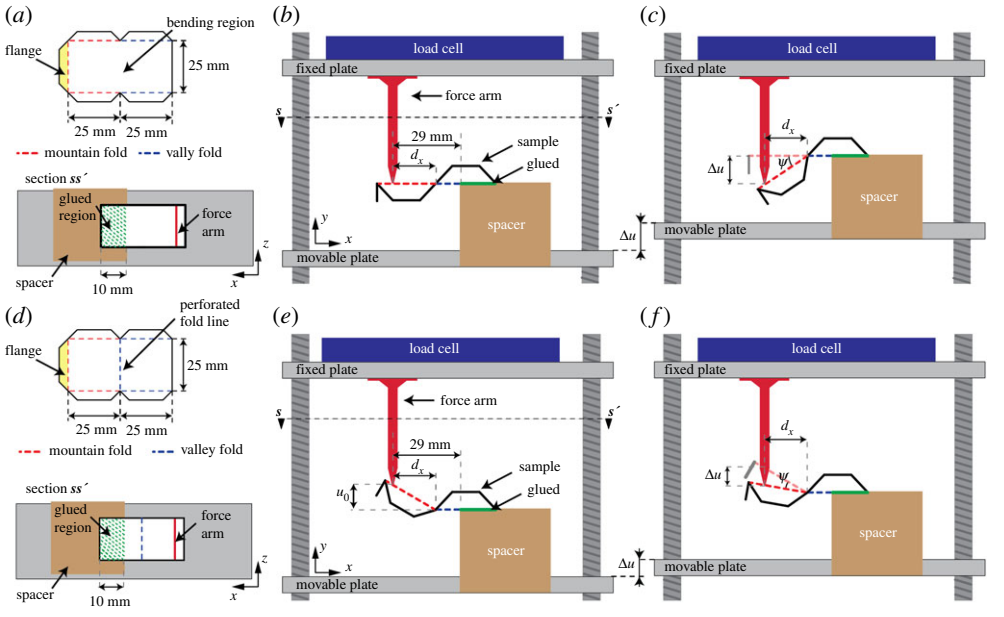

Figure 4. Schematics of the bending and folding test. (*a–c*) Characterization of the bending stiffness of the panels, and (*d–f*) characterization of the folding stiffness of the perforated crease (fold line). (Online version in colour.)

where d_x is the distance between the crease/bending line and the force arm (i.e. $d_x = 19$ mm), F is the measured force from load cell, and u_0 is the initial distance between the force arm and the spacer in the y-direction. For the measurements of bending stiffness, $u_0 = 0$, while for the folding stiffness, we see different initial neutral angles after a complete fold. In such cases, u_0 was measured for each sample based on where the force arm touches the sample. Figure 5 shows the moment-rotation diagrams of one bending test and one folding test for the craft paper. The measured rotational stiffness of all samples and materials are collected in tables 1–3, with coefficients of determination (i.e. R_B^2 and R_F^2) included. The coefficients of determination (i.e. R_F^2 and R_B^2) can be used to indicate the linearity of the constitutive relationships of the folding hinges and bending lines. We observe that while the bending constitutive relationships of all three materials are quite linear as all R_B^2's are close to 1.0, the linearity of the folding constitutive relationships is less significant. For the polyester film, the average value of R_F^2 is 0.88, less than the other two materials, which indicates a relatively strong nonlinear behaviour of the folding hinges of polyester films. On the contrary, both bending and folding constitutive of the craft paper are quite linear, even for a relatively large range of rotation, as implied by the coefficients of determination, and as shown in figure 5, which is the reason why later we use the properties of the craft paper to build our numerical models. The mean value of the measured rotational stiffness is normalized by the bending/folding hinge length (i.e. 25 mm) to obtain the rotational stiffness per unit length. The ratios between the bending and folding stiffness for the materials used in the experiments are averaged at $K_B/K_F = 6.4$, $K_B/K_F = 1.95$ and $K_B/K_F = 10.7$ for craft paper, polyester film, and the composite sheet, respectively. The ratio of K_B/K_F is a key parameter that determines whether an origami is close to a mechanism (rigid origami) or not. For example, when $K_B/K_F \to \infty$, we approach a situation where rigid panels are connected by frictionless hinges (rigid origami). When $K_B/K_F = 1$, the panel and the fold have the same stiffness (such as moulded samples).

(iii) Stretching stiffness

To obtain Young's modulus (E_S) of the three sheet materials, we use an Instron model 5566 equipped with a 30 kN load cell to perform tensile tests on five samples per material (figure 6).

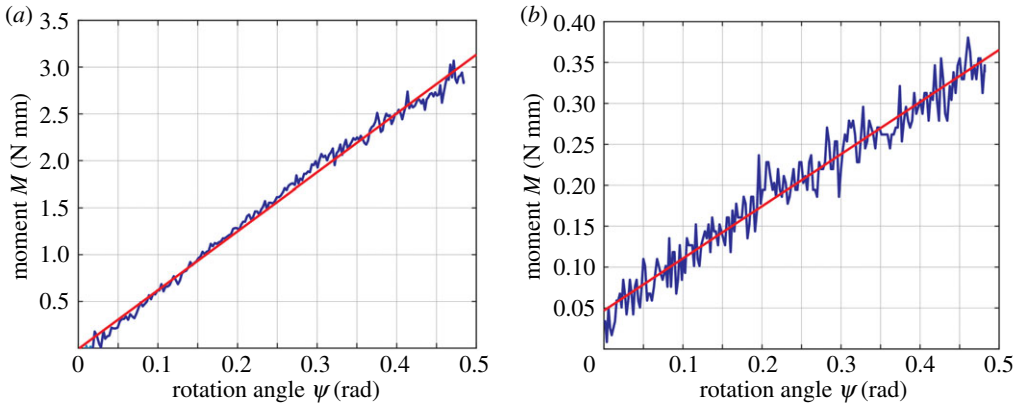

Figure 5. Moment M versus rotation angle ψ for the panel bending (*a*) and folding (*b*) from one sample made of Canson Mi-Teintes paper. The measured data are plotted in blue lines, and the red lines represent the linear regressions. From the slope of the red line, the rotational stiffness is obtained. (Online version in colour.)

Table 1. Canson Mi-Teintes properties.

E_S (MPa)	K_B (N · mm(rad · mm)$^{-1}$)	R_B^2	K_F (N · mm(rad · mm)$^{-1}$)	R_F^2
1313.3	0.2513	0.9934	0.0375	0.9226
1114.3	0.2078	0.9693	0.0322	0.9280
1287.0	0.2465	0.9923	0.0225	0.9520
1201.9	0.2141	0.9858	0.0434	0.9621
1180.5	0.2194	0.9930	0.0445	0.9489
average				
1219.4	0.2278	0.9868	0.0366	0.9427

Table 2. Grafix drafting film properties.

E_S (MPa)	K_B (N · mm(rad · mm)$^{-1}$)	R_B^2	K_F (N · mm(rad · mm)$^{-1}$)	R_F^2
2476.5	0.0809	0.9896	0.0401	0.8413
2480.5	0.0765	0.9904	0.0396	0.7753
2408.6	0.0896	0.9921	0.0466	0.9821
2423.0	0.0938	0.9839	0.0458	0.9310
2455.5	0.0900	0.9857	0.0481	0.9077
average				
2448.8	0.0862	0.9883	0.0441	0.8875

Each sample has a dimension of 20 mm × 100 mm. From those tests, we take the mean of the results and obtained the Young's modulus E_S. The data are collected in tables 1–3.

(b) Miura-ori sample fabrication

The crease patterns for the samples are generated by a Matlab program. We include a reference group consisting of six samples folded from standard Miura-ori pattern. For each choice of standard deviation for random perturbations, a group of 10 different crease patterns are generated. An electronic cutting machine (Silhouette CAMEO, Silhouette America) is used to

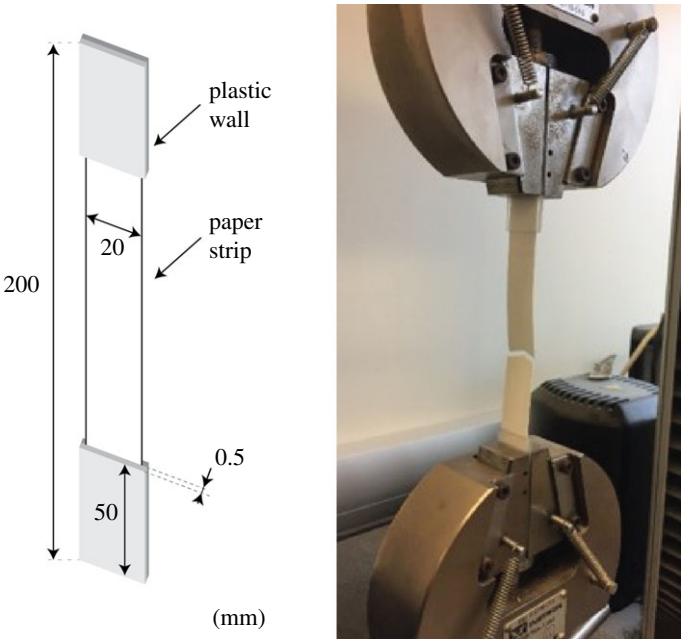

Figure 6. Tension test on paper material using the Instron machine. (Online version in colour.)

Table 3. Durilla durable premium ice card stock properties.

E_S (MPa)	K_B (N · mm(rad · mm)$^{-1}$)	R_B^2	K_F ((N · mm(rad · mm)$^{-1}$)	R_F^2
1317.1	0.7667	0.9895	0.0827	0.9797
1323.5	0.7587	0.9886	0.0623	0.9132
1298.3	0.7866	0.9892	0.062	0.9323
1277.2	0.7729	0.9889	0.069	0.9377
1297.0	0.7952	0.9841	0.0875	0.9032
average				
1302.6	0.7760	0.9881	0.0727	0.9332

fabricate samples from the craft paper, and a PLS4.75 laser cutting system (Universal laser systems) is used to fabricate samples from the polyester film and the composite sheet. Creases were patterned by cutting perforated lines with equal lengths of material and gaps. All samples are then carefully folded by hand, according to the same folding procedure. Samples are first folded to approximately 20% of the full extension of the crease pattern before mechanical testing, and then fit into a mould of partially folded configuration with width of $W_0 = 152$ mm for approximately 7 days to release the residual stresses. This results in a nominal rest fold angle at $\beta_0 = 95^\circ$.

(c) Experimental tests on the Miura-ori samples

The origami metamaterial samples are placed on the custom mechanical testing device between the two vertical steel plates by a distance of 152 mm. One of the plates is fixed and mounted on a high-sensitivity load cell (50 N); the other is controlled by a stepper motor to apply prescribed displacement load. To reduce friction, we apply some lubricant oil on all plates that have direct contact with the sample. On the edges of the Miura-ori samples, we also apply some graphite powder to further reduce friction in the transverse direction of compression. All samples are

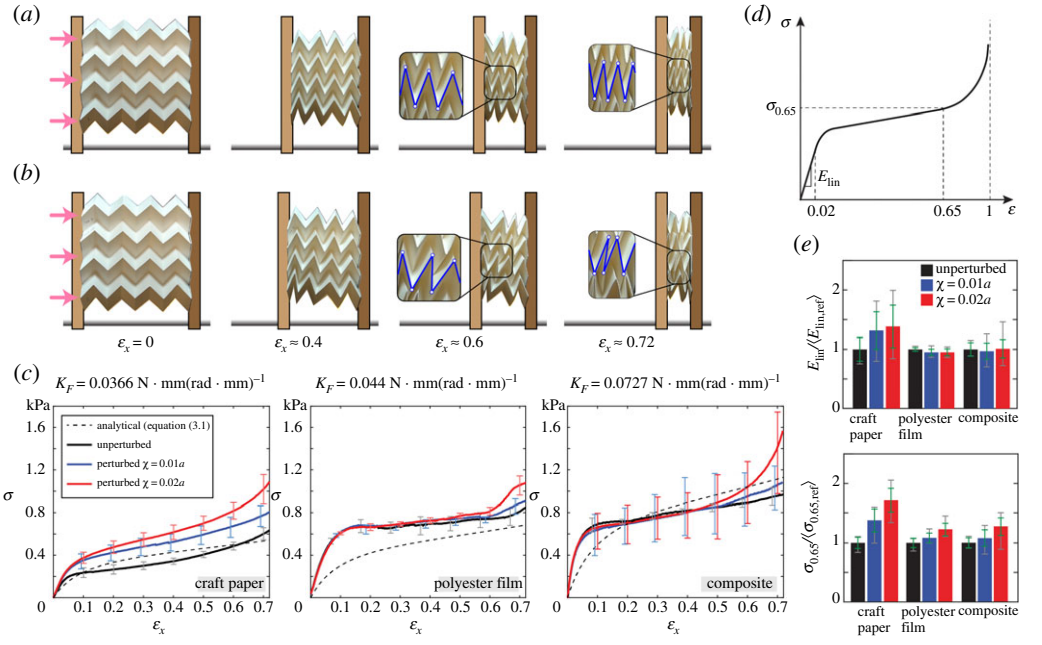

Figure 7. Experimental quantification of the effect of geometric imperfections (see electronic supplementary material, Movie S1). (*a*) Snapshots of an unperturbed sample (Craft paper). The blue lines outline a row of vertices. (*b*) Snapshots from experiment of a perturbed sample with $\chi = 0.02a$ under increasing compressive strain. (*c*) Bulk stress σ (kPa) versus compressive strain ε_x for samples made of different materials. The solid lines represent mean responses. The error bars show the maximum and minimum values of the measured σ data. Plotting the min max values can show that our data suggests no significant skewness, as the min and max values are about equidistance from the mean. The dashed line is the response of ideal Miura-ori according to equation (2.1), where K_F is obtained by mechanical test on single creases as elaborated in §3a(iii). (*d*) Illustration of the constitutive model. (*e*) E_{lin} and $\sigma_{0.65}$ for different sample groups, where $E_{\text{lin,ref}}$ and $\sigma_{0.65,\text{ref}}$ refers to unperturbed sample group. The grey error bars show standard deviations, and the green error bars indicate extrema of data. (Online version in colour.)

subject to a displacement load of 110 mm with speed of 1 mm s^{-1}. The displacement and force data are simultaneously recorded by a custom LabVIEW program, and stored for later analysis.

During the experiments, the samples are uniaxially compressed along the x-direction, as shown in figure 7*a*,*b*. The behaviour of the samples is recorded by the compressive strain ($\varepsilon_x = \Delta W/W_0$) and bulk stress ($\sigma = F/H_0L_0$, where F is the measured force, and H_0, L_0 and W_0 are dimensions of the initial configuration). As shown in figure 7*c*, all samples behave almost linearly up to a small strain around 2%. The metamaterials continue to deform at slowly increasing stress for a large range of deformation (plateau), until the stress rises with a notably increasing slope (densification).

To quantitatively compare the constitutive behaviour of Miura-ori, we define the initial linear modulus E_{lin}, computed as the slope of the stress–strain curve between zero and 2% strain, and the plateau stress $\sigma_{0.65}$ as the stress at 65% strain, as illustrated in figure 7*d*. The plateau stress is defined as the end-of-plateau stress. The representative strain of 65% is based on our observation on all curves as the approximate end point of the plateau stage before densification. Let us denote $\langle\cdot\rangle$ as the mean value operator. The reference groups of unperturbed samples have: $\langle E_{\text{lin,ref}}\rangle = 4.93$ kPa and $\langle\sigma_{0.65,\text{ref}}\rangle = 0.52$ kPa for the craft paper, $\langle E_{\text{lin,ref}}\rangle = 11.11$ kPa and $\langle\sigma_{0.65,\text{ref}}\rangle = 0.7$ kPa for the polyester film, and $\langle E_{\text{lin,ref}}\rangle = 18.33$ kPa and $\langle\sigma_{0.65,\text{ref}}\rangle = 0.92$ kPa for the composite sheet. Based on the results, we see that for all three materials, as χ increases, the Miura-ori become stiffer, as shown in figure 7*c*,*e*. Compared to the reference groups: for the craft paper samples, $\langle E_{\text{lin}}\rangle$ increases up to 38% and $\langle\sigma_{0.65}\rangle$ increases up to 72%; for the polyester

film samples, $\langle E_{\text{lin}} \rangle$ remains almost unchanged, but $\langle \sigma_{0.65} \rangle$ increases by 22%; for the composite samples, $\langle \sigma_{0.65} \rangle$ increases by 27%. We notice that the average value of linear moduli of the three types of experimental samples is less sensitive to geometric imperfections compared to the plateau stress, however, geometric imperfection increases their variances. This is likely due to material variabilities, such as the variances of K_F (see §3a(iii)). In addition, the edges of the imperfect Miura-ori samples are jagged, not as straight as the standard pattern. Hence, when the compression is applied by the moving plate, it is possible that the compression is not applied uniformly to the sample in the beginning, causing localized deformation of the protrusions first near the boundary before affecting the entire sample, which may appear a softer response on the load record.

Besides the difference in the global responses between perturbed and unperturbed samples, significant difference is also observed at the local level (cf. figure 7*a*,*b*). The unit cells of the unperturbed pattern uniformly deform with lattice structure of vertices remaining relatively ordered and periodic throughout the compressive folding process. The perturbed samples, however, display non-uniform deformation among unit cells, with severely distorted lattice structures, especially under higher compressive strains.

4. Numerical analyses

The variability of the mechanical properties of the physical samples comes from not only random geometric imperfections, but also material variabilities. To study the pure effect of geometric imperfections, we would like to exclude material variabilities as much as possible. Hence, we perform numerical simulations using a reduced order bar-and-hinge model of origami [36,37], as introduced earlier in figure 1*b*. The bar-and-hinge model represents the behaviour of an origami structure by a triangulated bar frame with constrained rotational hinges, capturing three essential deformation modes of origami structures: in-plane stretching (modelled by K_S), folding (modelled by K_F) and panel bending (modelled by K_B). With only a few degrees of freedom, the bar-and-hinge model predicts well the overall mechanical behaviour of elastic origami structures [7,9,26,35,36], offering the generality and computational efficiency that is needed to reveal statistical trends of the influence of random geometric imperfections. The numerical simulations are performed using the MERLIN software [36] that implements the bar-and-hinge model. Appendix A provides details about the implementation. We use the data collected from the craft paper to tune K_B and K_S of the bar and hinge model, and vary K_F to assess the effect of hinge compliance. The folding stiffness K_F is calculated based on different prescribed ratios of K_B/K_F.

Using numerical models, we are able to assign constant material properties and impose random imperfections under precise probability distributions. Omitting the process of folding, we configure the numerical models directly in three dimensions (figure 8*a*), and impose random nodal perturbation onto the three-dimensional model. This is to keep the study general because not all origami metamaterials are made by folding from a flat piece of sheet. Some are directly assembled to partially folded state by pieces of panels, yet they also carry geometric imperfections. Moreover, some types of imperfections, such as distortion induced by non-uniform thermal effect, may display strong spatial correlation. Thus, we introduce spatially correlated random fields [38] to generate the nodal perturbations. The random perturbations follow zero-mean Gaussian fields with an exponential covariance function [39] characterized by standard deviation χ and correlation length ℓ:

$$C(\boldsymbol{x}_i, \boldsymbol{x}_j) = \chi^2 \exp\left(-\frac{||\boldsymbol{x}_j - \boldsymbol{x}_i||}{\ell}\right), \tag{4.1}$$

where $||\boldsymbol{x}_j - \boldsymbol{x}_i||$ is the Euclidean distance between two nodes whose coordinates are $\boldsymbol{x}_i$ and $\boldsymbol{x}_j$. Larger ℓ indicates stronger spatial correlation between random nodal perturbations, as shown in figure 8*a*. For the experimental samples presented earlier, the imposed perturbations follow random fields with $\ell = 0$. We prepare, in total, 16 groups of perturbed samples with four different

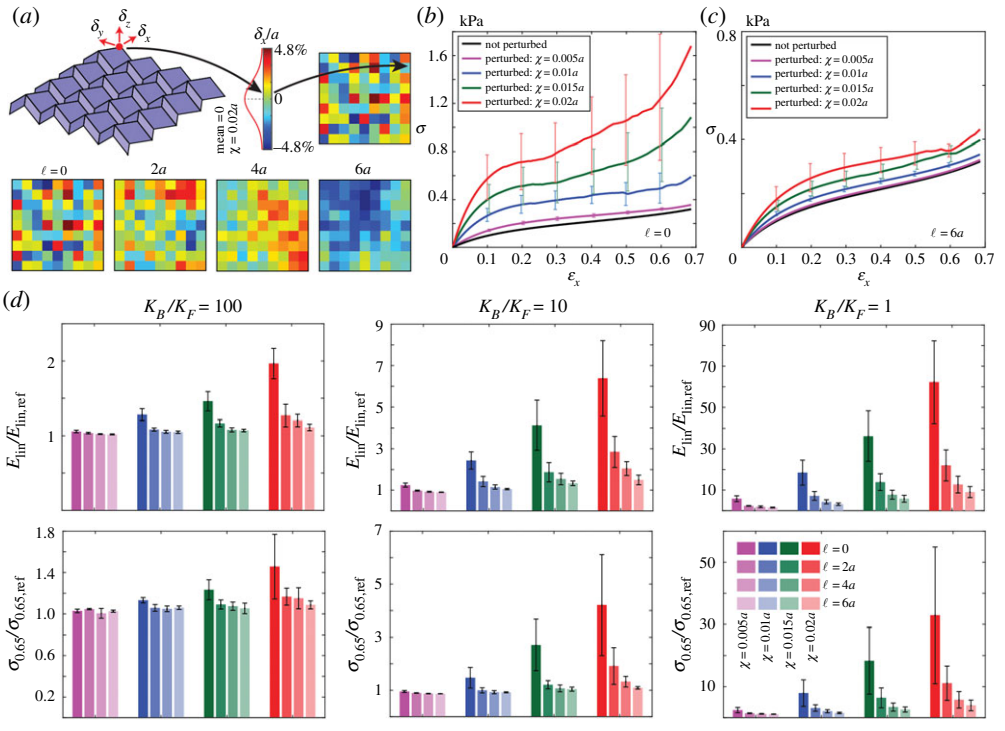

Figure 8. Numerical quantification of the effect of geometric imperfections (see electronic supplementary material, Movie S2). (*a*) Modelling of random geometric imperfections by random fields of nodal perturbations. At each node, the perturbation is decomposed into *x*-, *y*- and *z*- directions (denoted as δ_x, δ_y and δ_z), as we assume no directional preference of the geometric imperfections. The perturbations δ_x, δ_y and δ_z are samples independently from three random fields generated by the same statistical parameters, i.e. mean (= 0), standard deviation χ, and correlation length ℓ. The four coloured maps demonstrate how ℓ affects spatial correlation between nodal perturbations. (*b*,*c*) Bulk stress σ versus compressive strain ε_x for numerical samples with $K_B/K_F = 10$, showing (*b*) $\ell = 0$ and (*c*) $\ell = 6a$. Each solid line shows the mean response of a group of samples and the error bars extend to one standard deviation. The stress σ is in units of kPa. (*d*) E_{lin} and $\sigma_{0.65}$ of sample groups with different material parameters. Each black error bar extends to one standard deviation. The ratio of K_B/K_F reflects the relative stiffness between bending and folding deformations. For all cases, $a = b = 25$ mm, $\alpha = 60°$ and $\beta_0 = 70°$. (Online version in colour.)

χ's and four different ℓ's. We assume that the random field is homogeneous, because typically spatial variability in isotropic materials follows a homogeneous covariance law (depends only on spatial separation) [39]. In addition, some imperfections may be non-Gaussian in nature. Therefore, the adoption of Gaussian random field in this work is an idealized (and first attempt) approximation that intends to provide some insight into the influence of geometric imperfections.

For a group with a given combination of χ and ℓ, the number of samples are determined to ensure the estimated mean of $\sigma_{0.65}$ has 95% confidence to be within ±0.1 kPa from the true mean, using the following formula [39]:

$$N \geq \frac{\tilde{\chi}^2_{\sigma_{0.65}}}{w^2}\left(\Phi^{-1}\left(1-\frac{h}{2}\right)\right)^2, \tag{4.2}$$

where $w = 0.1$, $h = 0.05$ (for 95% confidence), $\tilde{\chi}_{\sigma_{0.65}}$ is the measured standard deviation of $\sigma_{0.65}$ of the samples, and Φ^{-1} is the inverse of the standard normal cumulative distribution function. Based on the variance of the measure samples, the number of samples of each group could be different. The number of samples increases by multiples of 8 to use parallel computation on eight cores. Each group has a minimum of eight samples and a maximum of 240 samples. For all cases, $a = b = 25$ mm, $\alpha = 60°$, and $\beta_0 = 70°$.

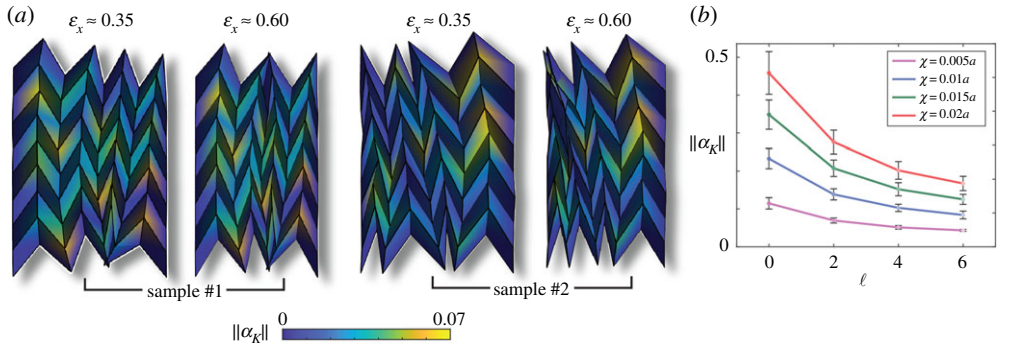

Figure 9. Quantification of geometric imperfections in terms of Kawasaki excess defined in §5. (*a*) Snapshots from numerical simulation of a perturbed sample with $\chi = 0.02a$ and $\ell = 0$. The varying colour indicates the absolute value of Kawasaki excess $||\alpha_K||$ at each vertex. (*b*) Change of global Kawasaki excess $||\alpha_K||$ as χ and ℓ vary. The error bars extend to one standard deviation. For all cases, $\alpha = 60°$, $\beta_0 = 70°$. (Online version in colour.)

A uniform displacement load is applied to compress the numerical samples (see electronic supplementary material, movie S2). As shown in figure 8, the $\sigma - \varepsilon_x$ curves of the numerical samples display a similar trend as the physical samples. While the change of $\sigma_{0.65}$ due to imperfection has the same trend as in the experimental data, the influence of imperfection on the linear modulus E_{lin} is more obviously presented in the numerical data, as shown in figure 8*b*,*c*. The deformation of imperfect numerical samples also displays obvious local disorder, as shown in figure 9*a*. The variances shown by the error bars come from the complex effect of random imperfections on origami-based metamaterials, as each numerical sample in the same group is imposed with different nodal perturbations drawn as one realization from the same underlying random field. We remark that the larger the standard deviation of the input random nodal perturbations, the larger the variances of the observed properties of the imperfect origami metamaterials, in agreement with the experimental data.

5. Relation between geometry and mechanical response

Both the experimental and numerical results reveal that the magnitude of nodal perturbations positively correlates to the stiffness of Miura-ori (see figures 7*e* and 8*d*). Furthermore, the numerical samples show that the spatial correlation between nodal perturbations contributes negatively to the increase of stiffness, as shown in figure 8*d*. To quantitatively describe geometric imperfections, we need a parameter that provides a consistent and continuous measure that reflects the effects of magnitude and spatial correlation. We could use (ℓ/χ) as the measure of geometric imperfection, as shown in figure 10. This ratio is independent of the size of the origami (quantified by panel edge length a), however, such measure may lead to ambiguities among sample groups with $\ell = 0$.

Owing to its simplicity and relevance, the Kawasaki excess [40] offers a good measure of the random geometric imperfection (as introduced in figure 1*c*). The Kawasaki theorem states that the flat-foldability of an origami vertex is equivalent to $\alpha_K = 0$ [40]. For a multi-vertex origami, we collect the vertex-wise α_K into a vector $\boldsymbol{\alpha}_K$, and define the Kawasaki excess of an multi-vertex origami as the L2-norm of the Kawasaki excess vector (i.e. $||\boldsymbol{\alpha}_K||$). It is sufficient that if $||\boldsymbol{\alpha}_K|| \neq 0$, the pattern loses global flat-foldability. As shown in figure 9*b*, $||\boldsymbol{\alpha}_K||$ increases as χ increases, and decreases as ℓ increases, reflecting similar effect of χ and ℓ on E_{lin} and $\sigma_{0.65}$. For an imperfect Miura-ori, as we keep compressing, the origami metamaterial becomes very stiff before it can be folded flat, indicating that its flat-foldability is destroyed by the random imperfections. Furthermore, as shown in figure 9*a*, at the local level, we can clearly see that origami vertices with higher Kawasaki excess appear to be stiffer in folding than vertices with smaller Kawasaki excess,

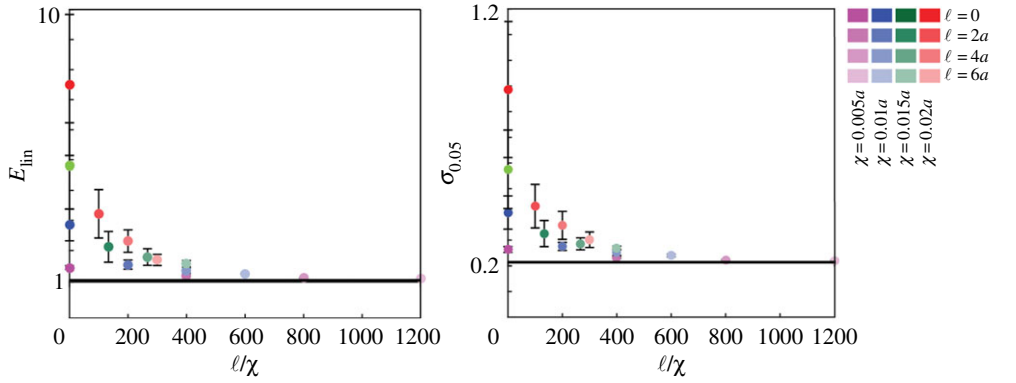

Figure 10. Mechanical properties versus relative imperfection measured as ℓ/χ. Each solid dot shows the mean response of a group of samples and the error bars extend to one standard deviation. The black solid line refers to the obtained values from the unperturbed Miura-ori. All samples in this figure have $\alpha = 60°$ and $\beta_0 = 70°$, $K_B/K_F = 10$. The E_{lin} and $\sigma_{0.65}$ are in units of kPa. (Online version in colour.)

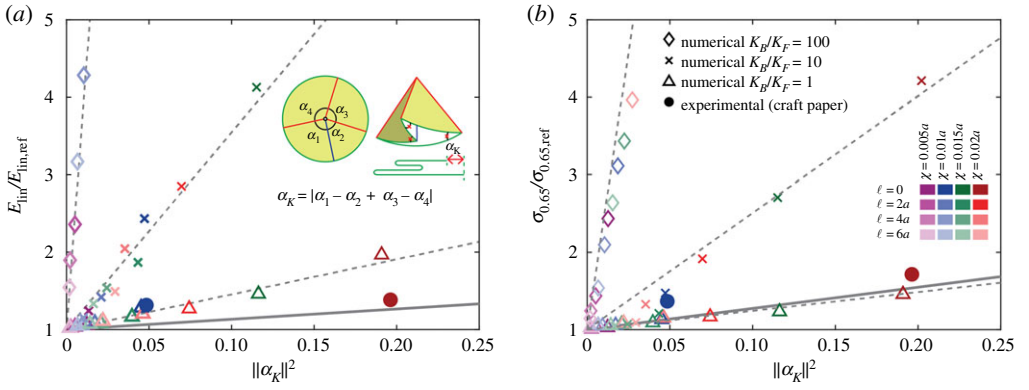

Figure 11. Connection between origami geometric design constraint with metamaterial mechanical properties. (*a*) The square of Kawasaki excess $||\alpha_K||^2$ versus the normalized mean values of E_{lin}. Each straight line is obtained from linear regression of all data points belonging the samples with the same material properties. The slopes of the linear trend lines are given by: $s_{E,\diamond} = 283.20$ ($K_B/K_F = 100$), $s_{E,\times} = 25.44$ ($K_B/K_F = 10$), $s_{E,\Delta} = 4.54$ ($K_B/K_F = 1$), $s_{E,\text{Exp}} = 1.33$ (Craft paper). Each marker represents the mean value E_{lin} of a certain group of samples. (*b*) The colours of the makers are explained in the inset legend. (*b*) The square of Kawasaki excess $||\alpha_K||^2$ versus the normalized mean values of $\sigma_{0.65}$. We obtain $s_{\sigma,\diamond} = 142.92$, $s_{\sigma,\times} = 15.07$, $s_{\sigma,\Delta} = 2.42$ and $s_{\sigma,Exp} = 2.74$. The shapes and colours of the makers are explained in the inset legends in (*b*). Notice that the linear regression is performed on all data points of a material, however, the dots only show the means of the clusters. (Online version in colour.)

contributing to the increase of global stiffness. *Therefore, we may conjecture that flat-foldability is a geometric feature that causes the change of mechanical properties of imperfect Miura-ori metamaterials.*

Indeed, we discover that both E_{lin} and $\sigma_{0.65}$ (normalized by the reference values based on unperturbed samples) correlate with the square of Kawasaki excess $\|\boldsymbol{\alpha}_K\|^2$, as shown in figure 11. The slope of each line reflects the sensitivity of samples made with the same materials to random geometric imperfections. Therefore, the average compressive modulus and plateau stress of geometrically imperfect Miura-ori can be estimated as

$$\frac{\langle E_{\text{lin}}\rangle}{E_{\text{lin, ref}}} = s_E||\boldsymbol{\alpha}_K||^2 + 1, \frac{\langle \sigma_{0.65}\rangle}{\sigma_{0.65,ref}} = s_\sigma||\boldsymbol{\alpha}_K||^2 + 1. \tag{5.1}$$

The samples with higher K_B/K_F ratio are more sensitive to geometric imperfections. The response of the craft paper samples (with $K_B/K_F = 6.8$) is expected to be between the lines of

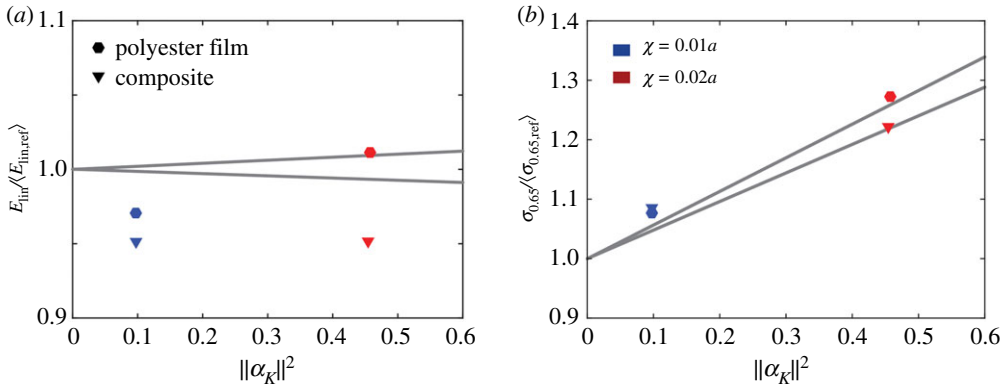

Figure 12. The normalized mean values of (*a*) E_{lin} and (*b*) $\sigma_{0.65}$ versus the square of Kawasaki excess $||\boldsymbol{\alpha}_K||^2$ for the polyester film samples and composite samples. The linear regression is performed on all data points of a material, however, the dots only show the means of the clusters. (Online version in colour.)

$K_B/K_F = 1$ and $K_B/K_F = 10$ from the numerical data (tuned by the properties of the craft paper), which is true for $\langle\sigma_{0.65}\rangle$ of the craft paper samples. However, the sensitivity of experimental samples is generally lower than what we expected for both $\langle\sigma_{0.65}\rangle$ and $\langle E_{lin}\rangle$. There are several possible reasons. First, in the numerical models, the creases always hold their continuity, while in the physical models, the perforated creases (especially their intersecting nodes) can be pulled apart by small gaps, which compensate for the violation of strong kinematic constraint imposed by the geometric continuity, and thus mitigate the effect of geometric imperfection (figure 2). Second, the numerical models are elastic while the physical models are inelastic. Lastly, the material variabilities could also be a contributing factor for this discrepancy, as it reduces the statistical significance of observations related to geometric imperfections.

Although not compared with the numerical model as the material parameters (i.e. K_S and K_B) in the numerical models are tuned only with the craft paper, similar linear correlation is seen in the polyester film samples and composite samples, as shown in figure 12. For the experimental samples made with three different materials, the correlations between the pair of $\langle E_{lin}\rangle$ and $||\boldsymbol{\alpha}_K||^2$ are not as strong as the pair of $\langle\sigma_{0.65}\rangle$ and $||\boldsymbol{\alpha}_K||^2$, while the numerical samples present clear correlations for both pairs. This discrepancy seems to suggest that the influence of geometric imperfections is more obvious at larger strains in practice.

The statistical correlation between E_{lin} (or $\sigma_{0.65}$) and $||\boldsymbol{\alpha}_K||^2$ does not imply the cause and effect relation between flat-foldability and stiffness of the Miura-ori. In an effort to explain such correlation, we conjecture that the violation of flat foldability causes the increase of compressive stiffness, and we derive that the amount of extra stored energy due to imperfection is proportional to $||\boldsymbol{\alpha}_K||^2$. Hence, the linear relationship between E_{lin} and $||\boldsymbol{\alpha}_K||^2$ (or $\sigma_{0.65}$ and $||\boldsymbol{\alpha}_K||^2$) follows.

To make sense of the correlation between E_{lin} (or $\sigma_{0.65}$) and $||\boldsymbol{\alpha}_K||^2$, we consider the following deformation procedure to achieve a certain amount of compressive folding (figure 13*a–d*): (i) enforce the geometry of the distorted panels to the standard panel shapes by in-plane deformation; (ii) compress the origami structure by pure folding; (iii) release the in-plane strains and allow the structure to find new equilibrium between folding, bending and stretching. In step (ii), the structure deforms following the same kinematics as an ideal rigid origami, thus the extra strain energy in the system after this step comes from the deformation in step (i). In step (iii), finding the new equilibrium leads to a lower or equal energy state compared to step (ii). Considering continuum elastic panels with small geometric imperfection, we may approximate the extra strain energy compared to the ideal pattern around a vertex k as (considering a circular disc of radius r),

$$\Delta U_k = \eta_k \int_0^a \frac{1}{2} E_S t \sum_m \left(\frac{(\delta_m \alpha_K)^2 r}{\alpha_m} \right) \mathrm{d}r, \tag{5.2}$$

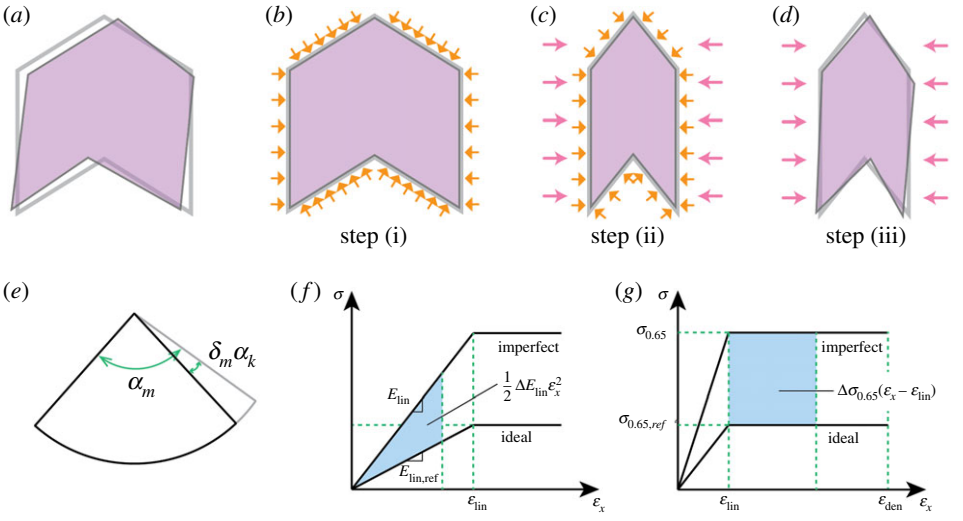

Figure 13. Schematic of a hypothetical deformation process of imperfect origami. (*a*) The purple pattern indicates the imperfect geometry, and the grey lines indicate the ideal geometry. (*b–d*) Step (i) to (iii). The orange arrows imply the enforced deformation field, which confines the imperfect geometry to the ideal geometry. The pink arrows imply applied displacements on the pattern. (*e*) An imperfect single vertex with angular deficit ($\delta_m\alpha_K$). (*f*) Additional strain energy induced by imperfection when $\varepsilon_x \leq \varepsilon_{\text{lin}}$. (*g*) Additional strain energy induced by imperfection when $\varepsilon_{\text{lin}} < \varepsilon_x \leq \varepsilon_{\text{den}}$. (Online version in colour.)

where t is the thickness of panels, and $(\delta_m\alpha_K)$ is the angular excess or deficit of each sector angle m around vertex k (figure 13*e*). The relaxation factor η_k is a factor depending on both material and geometric properties of the system, such as K_B/K_S, K_B/K_F, and folding angles between panels, etc. In equation (5.2), α_K, δ_m and η_k are random variables. We assume that δ_m and η_k are independent from α_K. Taking the expectation ($\langle . \rangle$) of both sides of equation (5.1), we can obtain that:

$$\langle \Delta U_k \rangle \approx \langle \alpha_k^2 \rangle \left\langle \eta_k \int_0^1 \frac{1}{2} E_S t \sum_m \left(\frac{\delta_m^2 r}{\alpha_m} \right) \mathrm{d}r \right\rangle \propto \langle \alpha_k^2 \rangle. \tag{5.3}$$

The actual deformation of imperfect Miura-ori is more complex than the aforementioned three steps, and thus equation (5.3) is only hypothetical. Nevertheless, assuming elasticity, the simplified procedure helps to shed some light on the linear correlation between ΔU_K and α_K^2. Since equation (5.3) applies to all vertices within an origami, we can take a sum over a finite number of k, which leads to:

$$\sum_k \langle \Delta U_k \rangle = \left\langle \sum_k \Delta U_k \right\rangle \propto \sum_k \langle \alpha_k^2 \rangle = \langle ||\boldsymbol{\alpha}_K||^2 \rangle, \tag{5.4}$$

where $\sum_k \Delta U_k$ is the global (total) strain energy difference.

Denoting $\Delta E_{lin} = E_{\text{lin}} - E_{\text{lin,ref}}$, for $\varepsilon_x \leq \varepsilon_{\text{lin}}$ (assuming $\varepsilon_{\text{lin}} = 0.02$), on the global scale we obtain:

$$\frac{1}{2}\langle \Delta E_{\text{lin}} \rangle \varepsilon_x^2 \approx \left\langle \frac{\sum_k \Delta U_k}{W_0 H_0 L_0} \right\rangle = \frac{\langle \sum_k \Delta U_k \rangle}{W_0 H_0 L_0}, \tag{5.5}$$

where $W_0H_0L_0$ is the initial volume of the Miura-ori, and $E_{\text{lin,ref}}$ is obtained from the reference pattern without geometric imperfections (figure 13*f*). Therefore, we may conclude that for a group of samples with the same geometric feature and material properties, under random *geometric imperfections*, $\langle \Delta E_{lin} \rangle \propto \langle ||\boldsymbol{\alpha}_K||^2 \rangle$.

Similarly, when $\varepsilon_{\text{lin}} < \varepsilon_x \leq \varepsilon_{\text{den}}$ (assuming $\varepsilon_{\text{den}} = 0.65$), we have

$$\langle \Delta\sigma_{0.65}(\varepsilon_x - \varepsilon_{\text{lin}}) \rangle \approx \left\langle \frac{\sum_k \Delta U_k}{W_0 H_0 L_0} - \frac{1}{2}\Delta E_{\text{lin}} \varepsilon_{\text{lin}}^2 \right\rangle = \frac{\langle \sum_k \Delta U_k \rangle}{W_0 H_0 L_0} - \frac{1}{2}\langle \Delta E_{\text{lin}} \rangle \varepsilon_{\text{lin}}^2. \tag{5.6}$$

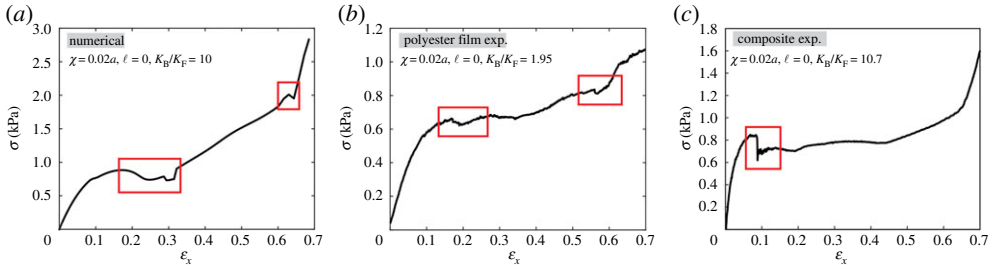

Figure 14. Examples of unstable strain softening, highlighted by red boxes, on perturbed Miura-ori metamaterials from (*a*) numerical and (*b*,*c*) experimental measurements. For perturbed samples with small χ or large ℓ, this phenomenon is rarely seen. Instability seems to be induced by relatively large geometric imperfections. (Online version in colour.)

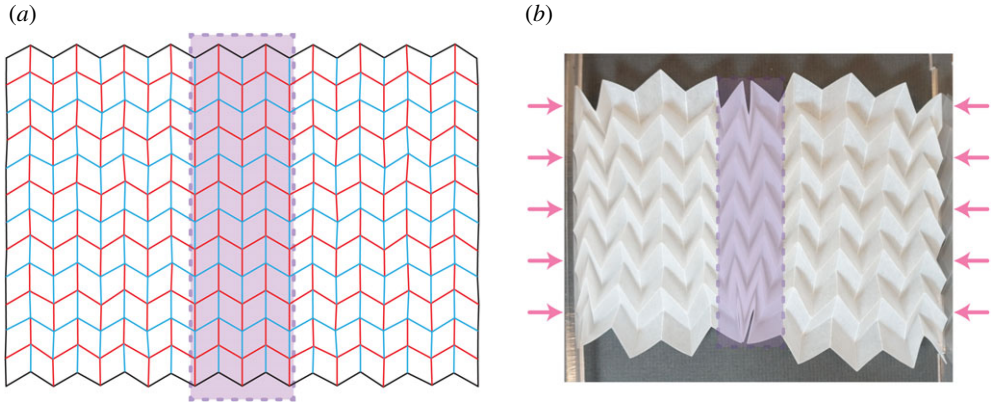

Figure 15. Purposely induced local deformation concentration by random perturbations. (*a*) The crease pattern. The blue lines are valley folds and the red lines are mountain folds. The purple region represents unperturbed portion. (*b*) The folded pattern under compression. Notice that the unperturbed region contracts more in the lateral direction than the perturbed portion because of the negative Poisson's ratio of Miura-ori. (Online version in colour.)

where $\Delta\sigma_{0.65} = \sigma_{0.65} - \sigma_{0.65,\mathrm{ref}}$ (figure 13*g*). Based on observation from both experiments and numerical simulations, it seems that ε_{lin} (= 0.02) is independent of $||\boldsymbol{\alpha}_K||$, ΔE_{lin}, and $\Delta\sigma_{0.65}$. Now we can derive that:

$$\langle \Delta\sigma_{0.65}(\varepsilon_x - \varepsilon_{lin})\rangle = \langle \Delta\sigma_{0.65}\rangle(\varepsilon_x - \varepsilon_{\mathrm{lin}}) = \frac{\langle \sum_k \Delta U_k\rangle}{W_0 H_0 L_0} - \frac{1}{2}\langle \Delta E_{\mathrm{lin}}\rangle \varepsilon_{\mathrm{lin}}^2, \tag{5.7}$$

which suggests that $\langle \Delta\sigma_{0.65}\rangle \propto ||\boldsymbol{\alpha}_K||^2$.

6. Other observations related to geometric imperfections

Another interesting phenomenon that we observed is that a relatively large degree of random geometric imperfections may lead to instability, as we observe strain softening from some polyester film samples, composite sheet samples, and numerical samples (figure 14). Such phenomenon shows a connection with the observations by Dudte *et al.* [20] that the flat-foldability residual (defined similarly to the Kawasaki excess) enables energy barrier between two configurations during form-find of curved Miura patterns.

In addition, we find no significant change of effective global in-plane Poisson's ratio due to imperfections, based on the numerical analyses. However, it is difficult to make a clear argument about the effect on Poisson's ratio, as the local distortion can be quite large (figures 5 and 7). As a result, based on the size of the local region over which Poisson's ratio is defined, we could reach at different conclusions. However, we remark that these are not the main focus of this paper, they

are mentioned here to demonstrate the complex influence of random geometric imperfections on the behaviour of origami-based metamaterials.

7. Conclusion and outlook

In conclusion, small random geometric imperfections change the mechanical properties of origami-based metamaterials. In this work, quantitative investigation is carried out by a representative case study on the popular Miura-ori, which serves as the building block for many origami-based metamaterials. Therefore, our results have direct implication on all Miura-ori based metamaterials. Moreover, the conceptual framework introduced in this research can potentially be extended to other patterns, such as the metric of Kawasaki excess for flat-foldable patterns. For non-flat-foldable pattern, the Kawasaki excess maybe rewritten as the difference between the Kawasaki excess of an imperfect pattern and its standard version. However, to obtain the exact properties of a piece of imperfect origami-based metamaterial, a thorough case study is always needed.

We conduct experimental and numerical analyses to reveal that small geometric imperfections may significantly increase the compressive stiffness of Miura-ori. Owing to the random nature of the geometric imperfections, we notice relatively large standard deviations in observations, which is part of the physics of the problem being investigated. Because it is not representative to look at specific properties of each individual imperfect sample, in this research, we focus on the statistical average behaviour of imperfect samples. Indeed, we are able to find shared trends among imperfect samples made with different materials, both experimentally and numerically, which helps us to make general predictions on the influence of geometric imperfections. *In particular, we find that the increases of the linear modulus and plateau stress of imperfect Miura-ori metamaterial correlate to the square of its Kawasaki excess, which is a purely geometric metric based on the vertex sector angles that reflects the degree of imperfections*.

In addition, the induced large variance of performance by random geometric imperfections in origami-based metamaterials is another important point that we would like to draw attention. We notice that, a higher degree of random geometric imperfections significantly amplifies the variance of the mechanical properties of origami-based metamaterials, which is in general undesirable, and has to be considered cautiously in applications. However, for applications such as energy storage and dissipation [41,42], geometric imperfections may be beneficial as they generally raise stored energy (i.e. area below the $\sigma - \varepsilon_x$ curve) in the material under the same amount of deformation. Furthermore, one may exploit random geometric imperfections to purposely modify the behaviour of origami-based metamaterials, similar to intentional imperfections [18,31]. For example, we can introduce unevenly distributed imperfections to achieve functionally graded stiffness (like figure 1*a*), or create designated local deformations (figure 15). Moving forward, much work remains to be done, for instance, investigating the effect of geometric imperfections modelled by different random fields, for other deformation modes and origami patterns, in order to bring the theoretical advantages of origami [43] to real applications.

Data accessibility. All data used to generate these results are available in the main text. Further details could be obtained from the corresponding authors upon request.

Authors' contributions. K.L., P.G. and G.H.P. designed the research. K.L. and L.S.N. performed the experiments and simulations, conceived the mathematical models, interpreted results and analysed data. P.G. and G.H.P. provided guidance throughout the research. All the authors participated in manuscript writing and approved the manuscript for publication.

Competing interests. The authors declare no competing interest.

Funding. This work was support by the US National Science Foundation (NSF) through grant no. 1538830, the China Scholarship Council (CSC), the Brazilian National Council for Scientific and Technological Development (CNPq), and the Raymond Allen Jones Chair at Georgia Tech.

Acknowledgements. We thank the CEE machine shop at Georgia Tech for fabricating the mechanical testing bed. We appreciate the useful comments provided by Dr Americo Cunha from Rio de Janeiro State University. We thank Dr Diego Misseroni for his invaluable help on the cover image.

Appendix A. Nonlinear analysis using the bar-and-hinge model

The main goal of this appendix is to explain the nonlinear solver for displacement loading, as it is first documented in this paper, which is quite different from the solver for force loading published before [36]. In addition, we would like to provide details about the implementation of MERLIN in this research, to provide guidance to later research about the influence of geometric imperfections in origami metamaterials and structures.

The bar-and-hinge model can represent generically any origami structure by properly assigned constitutive models for stretching, folding and bending, regardless of the system being continuum or discrete. Here, we briefly describe the nonlinear elastic formulation of the bar-and-hinge method [36,37,44]. We consider a discretized origami structure as an elastic system. The total stored energy (Π) of the system has contributions from the bars (U_S), bending hinges (U_B) and folding hinges (U_F), which is written as:

$$\Pi(\boldsymbol{u}) = U_S(\boldsymbol{u}) + U_B(\boldsymbol{u}) + U_F(\boldsymbol{u}). \tag{A 1}$$

All terms are nonlinear functions of the nodal displacements $\boldsymbol{u}$. Equilibrium is obtained when Π is local stationary, and therefore the internal force vector ($\mathbf{T}$) and the tangent stiffness matrix ($\mathbf{K}$) can be derived as [9,36]:

$$\mathbf{T}(\boldsymbol{u}) = \mathbf{T}_S(\boldsymbol{u}) + \mathbf{T}_B(\boldsymbol{u}) + \mathbf{T}_F(\boldsymbol{u}) \tag{A 2}$$

and

$$\mathbf{K}(\boldsymbol{u}) = \mathbf{K}_S(\boldsymbol{u}) + \mathbf{K}_B(\boldsymbol{u}) + \mathbf{K}_F(\boldsymbol{u}), \tag{A 3}$$

where

$$\mathbf{T}_S(\boldsymbol{u}) = \frac{\partial U_S(\boldsymbol{u})}{\partial \boldsymbol{u}}, \mathbf{T}_B(\boldsymbol{u}) = \frac{\partial U_B(\boldsymbol{u})}{\partial \boldsymbol{u}}, \mathbf{T}_F(\boldsymbol{u}) = \frac{\partial U_F(\boldsymbol{u})}{\partial \boldsymbol{u}} \tag{A 4}$$

and

$$\mathbf{K}_S(\boldsymbol{u}) = \frac{\partial^2 U_S(\boldsymbol{u})}{\partial \boldsymbol{u}^2}, \mathbf{K}_B(\boldsymbol{u}) = \frac{\partial^2 U_B(\boldsymbol{u})}{\partial \boldsymbol{u}^2}, \mathbf{K}_F(\boldsymbol{u}) = \frac{\partial^2 U_F(\boldsymbol{u})}{\partial \boldsymbol{u}^2}. \tag{A 5}$$

As customary, the system equilibrium and tangent stiffness are summations of elemental contributions.

(a) Constitutive models

For each bar element, we define its stored energy as:

$$\varphi_S = AL_b\mathcal{W}(E_{xx}), \tag{A 6}$$

where A denotes member area, L_b denotes member length, and $\mathcal{W}$ is the energy density as a function of the one-dimensional Green–Lagrange strain E_{xx}. We adopt a one-dimensional Ogden model [45] for $\mathcal{W}$ such that

$$\mathcal{W}(E_{xx}) = \frac{E_S}{\gamma_1 - \gamma_2}\left(\frac{\lambda_1(E_{xx})^{\gamma_1} - 1}{\gamma_1} + \frac{\lambda_1(E_{xx})^{\gamma_2} - 1}{\gamma_2}\right), \tag{A 7}$$

where E_S is the initial modulus of elasticity, γ_1 and γ_2 are material constants taken as 5 and 1 [36]. The principle stretch λ_1 is a function of E_{xx} given by $\lambda_1 = (2E_{xx} + 1)^{-1/2}$. For small strains, the constitutive model approximates a linear elastic behaviour (figure 16*a*), which occurs in our simulations, as the strains of bar elements are very small. However, a nonlinear constitutive model is more robust for numerical computation [36]. In the numerical simulations, we use Young's modulus E_S of the Craft paper material, measured experimentally as described in §3a(iii).

Bar areas are defined uniformly considering average hinge width as shown in figure 16*b*:

$$A = \frac{(a+b)t\sin\alpha}{2}, \tag{A 8}$$

where $t = 0.24$ mm, which is measured from the craft paper material we used for the experiments.

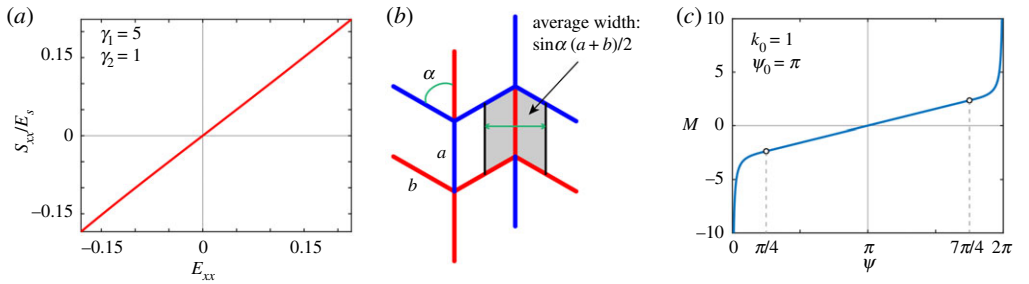

Figure 16. Constitutive models for bars and hinges. (*a*) Hyperelastic constitutive model for bar elements, shown by S_{xx} (normalized by the initial modulus of elasticity E_S) versus E_{xx} diagram. (*b*) Average width of the tributary area of bar elements, used to approximate the area of bars. (*c*) Enhanced linear elastic constitutive model for rotational springs, including bending and folding, plotted as M versus ψ diagram. The two black circles indicate the corresponding behaviour at ψ_1 and ψ_2. (Online version in colour.)

Bending and folding hinges are unified as rotational spring elements for which we adopted an enhanced linear constitutive model [36]. The expression for the resistive moment M per unit length (along axis) of the rotational spring is given as a function of rotational angle ψ, plotted in figure 16*c*:

$$M(\psi) = \begin{cases} k_0(\psi_1 - \psi_0) + \left(\dfrac{2k_0\psi_1}{\pi}\right)\tan\left[\dfrac{\pi(\psi - \psi_1)}{2\psi_1}\right], & 0 < \psi < \psi_1; \\ k_0(\psi - \psi_0), & \psi_1 < \psi < \psi_2; \\ k_0(\psi_2 - \psi_0) + \left(\dfrac{2k_0(2\pi - \psi_2}{\pi}\right)\tan\left[\dfrac{\pi(\psi - \psi_1)}{2\psi_1}\right], & \psi_2 < \psi < 2\pi. \end{cases} \tag{A 9}$$

Extremely high stiffness occurs when the dihedral angle approaches 0 or 2π, which prevents local penetration of panels. The stiffening effect when two adjacent panels are close to contact can be experienced in practice. In this work, we assume that $\psi_1 = \pi/4$ and $\psi_2 = 7\pi/4$. The bending and folding hinges are distinguished by different values of the linear stiffness k_0.

(b) Solving the nonlinear equilibrium problem

In the case of displacement loading, we denote the displacement load as $\boldsymbol{u}_p$, which is imposed on some d.f. of the system p. Some other d.f. (denoted as r) are fixed to provide support to the structure, and the corresponding displacement is $\boldsymbol{u}_r$, which is always a zero vector. The other d.f. in the system are free to move, denoted as f. Therefore, we partition the displacement field of the system into three groups: $\boldsymbol{u}_p$, $\boldsymbol{u}_r$ and $\boldsymbol{u}_f$. Among the three, $\boldsymbol{u}_p$ and $\boldsymbol{u}_r$ are boundary conditions and thus have fixed values. Notice that $\boldsymbol{u}_p$ is fixed but non-zero, while $\boldsymbol{u}_r$ is fixed to a zero vector.

We can also divide the internal force vector $\mathbf{T}$ into three parts by their corresponding d.f.: $\mathbf{T}_r$, $\mathbf{T}_p$ and $\mathbf{T}_f$. In an equilibrium state of the system, $\mathbf{T}_f = 0$ while the other two parts shall not be zero. The reaction forces of the supports are equal to $-\mathbf{T}_r$, and the external forces required to achieve the prescribed displacement $\boldsymbol{u}_p$ are given by $-\mathbf{T}_p$. After a displacement load $\boldsymbol{u}_p$ is applied, our goal is to find a proper $\boldsymbol{u}_f$, such that $\mathbf{T}_f(\boldsymbol{u}) = 0$, that is, all the internal free nodes are balanced.

We use a numerical algorithm to solve the nonlinear system of equations $\mathbf{T}_f(\boldsymbol{u}) = 0$. A large displacement load cannot be applied at once, otherwise a numerical algorithm would likely fail to converge. Hence, we divide the total displacement load into small increments. At each increment, we solve for the equilibrium using the Newton–Raphson method iteratively. Let i be the increment number, and j be the iteration number, denoted as $\boldsymbol{u}^{i,j}$. The prescribed amount of displacement load is $\boldsymbol{u}_p$, and the small displacement load applied at each increment is $\lambda^i \boldsymbol{u}_p$. When one or more partitions of $\boldsymbol{u}$ (i.e. $\boldsymbol{u}_p$, $\boldsymbol{u}_r$ and $\boldsymbol{u}_f$) are changed, $\boldsymbol{u}$ updates accordingly with the other

components remaining the same. We summarize the process in algorithm 1. The parameters λ^0, *tol*, j_{max}, and $N_{att,max}$ are predefined with values equal to 0.002, 10^{-6}, 50 and 5, respectively. The adaptive control over incremental step λ^i and damping factor υ is based on heuristic rules.

Algorithm 1 Large Displacement Load Solver

$u^{0,0} \leftarrow 0$, $i \leftarrow 1$, $\lambda^1 \leftarrow \lambda^0$, $\upsilon \leftarrow 1$, $N_{att} \leftarrow 0$
while $\sum_i \lambda^i < 1$ **do**
  $u_p^{i,0} \leftarrow u_p^{i-1,0} + \lambda^i u_p$
  $j \leftarrow 1$, $err \leftarrow 1$
  while $err > tol$ **do**
    $j \leftarrow j + 1$
    $T^{i,j-1} \leftarrow T(u^{i,j-1})$, $K^{i,j-1} \leftarrow K(u^{i,j-1})$
    $R^{i,j-1} \leftarrow -T^{i,j-1}$
    Solve $K_{ff}^{i,j-1} \Delta u_f^{i,j-1} = R_f^{i,j-1}$
    $u_f^{i,j} \leftarrow u_f^{i,j-1} + \upsilon \Delta u_f^{i,j-1}$
    $err \leftarrow \|\Delta u_f^{i,j-1}\|$
  end while
  if $j > (j_{max}/(\upsilon + 1))$ **then**
    $N_{att} \leftarrow N_{att} + 1$
    if $N_{att} < N_{att,max}$ **then**
      $\lambda^i \leftarrow 0.5\lambda^{i-1}$
    else
      $\lambda^i \leftarrow 1.5\max(\lambda^0, \lambda^{i-1})$
      $\upsilon \leftarrow 0.75\upsilon$
    end if
  else
    $\upsilon \leftarrow 1$, $N_{att} \leftarrow 0$
    $i \leftarrow i + 1$
    if $\lambda^i < \lambda^0$ **then**
      $\lambda^i \leftarrow \min(1.1\lambda^{i-1}, \lambda^0)$
    else
      $\lambda^i \leftarrow \max(0.9\lambda^{i-1}, \lambda^0)$
    end if
  end if
end while

References

1. Meza LR, Zelhofer AJ, Clarke N, Mateos AJ, Kochmann DM, Greer JR. 2015 Resilient 3D hierarchical architected metamaterials. *Proc. Natl. Acad. Sci. USA* **112**, 11 502–11 507. (doi:10.1073/pnas.1509120112)

2. Rocklin DZ, Chen BG, Falk M, Vitelli V, Lubensky TC. 2016 Mechanical Weyl modes in topological Maxwell lattices. *Phys. Rev. Lett.* **116**, 135503. (doi:10.1103/PhysRevLett.116.135503)
3. Matlack KH, Bauhofer A, Krödel S, Palermo A, Daraio C. 2016 Composite 3D-printed metastructures for low-frequency and broadband vibration absorption. *Proc. Natl. Acad. Sci. USA* **113**, 8386–8390. (doi:10.1073/pnas.1600171113)
4. Bertoldi K, Vitelli V, Christensen J, van Hecke M. 2017 Flexible mechanical metamaterials. *Nat. Rev. Mater.* **2**, 17066. (doi:10.1038/natrevmats.2017.66)
5. Liu K, Tachi T, Paulino GH. 2019 Invariant and smooth limit of discrete geometry folded from bistable origami leading to multistable metasurfaces. *Nat. Commun.* **10**, 4238. (doi:10.1038/s41467-019-11935-x)
6. Pratapa PP, Liu K, Paulino GH. 2019 Geometric mechanics of origami patterns exhibiting Poisson's ratio switch by breaking mountain and valley assignment. *Phys. Rev. Lett.* **122**, 155501. (doi:10.1103/PhysRevLett.122.155501)
7. Schenk M, Guest SD. 2013 Geometry of Miura-folded metamaterials. *Proc. Natl Acad. Sci. USA* **110**, 3276–3281. (doi:10.1073/pnas.1217998110)
8. Wei ZY, Guo ZV, Dudte L, Liang HY, Mahadevan L. 2013 Geometric mechanics of periodic pleated origami. *Phys. Rev. Lett.* **110**, 215501. (doi:10.1103/PhysRevLett.110.215501)
9. Filipov ET, Tachi T, Paulino GH. 2015 Origami tubes assembled into stiff, yet reconfigurable structures and metamaterials. *Proc. Natl. Acad. Sci. USA* **112**, 12 321–12 326. (doi:10.1073/pnas.1509465112)
10. Yasuda H, Yang J. 2015 Reentrant origami-based metamaterials with negative poisson's ratio and bistability. *Phys. Rev. Lett.* **144**, 185502. (doi:10.1103/PhysRevLett.114.185502)
11. Lv C, Krishnaraju D, Konjevod G, Yu H, Jiang H. 2014 Origami based mechanical metamaterials. *Sci. Rep.* **4**, 5979. (doi:10.1038/srep05979)
12. Pratapa PP, Suryanarayana P, Paulino GH. 2018 Bloch wave framework for structures with nonlocal interactions: application to the design of origami acoustic metamaterials. *J. Mech. Phys. Solids* **118**, 115–132. (doi:10.1016/j.jmps.2018.05.012)
13. Waitukaitis S, Menaut R, Chen BG, van Hecke M. 2015 Origami multistability: from single vertices to metasheets. *Phys. Rev. Lett.* **114**, 055503. (doi:10.1103/PhysRevLett.114.055503)
14. Fang H, Wang KW, Li S. 2017 Asymmetric energy barrier and mechanical diode effect from folding multi-stable stacked-origami. *Extreme Mech. Lett.* **17**, 7–15. (doi:10.1016/j.eml.2017.09.008)
15. Silverberg JL, Na JH, Evans AA, Liu B, Hull TC, Santangelo CD, Lang RJ, Hayward RC, Cohen I. 2015 Origami structures with a critical transition to bistability arising from hidden degrees of freedom. *Nat. Mater.* **14**, 389–393. (doi:10.1038/NMAT4232)
16. Wang LC, Song WL, Zhang YJ, Qu MJ, Zhao Z, Chen M, Yang Y, Chen H, Fang D. 2020 Active reconfigurable tristable square-twist origami. *Adv. Funct. Mater.* **30**, 1909087. (doi:10.1002/adfm.201909087)
17. Thota M, Li S, Wang KW. 2017 Lattice reconfiguration and phononic band-gap adaptation via origami folding. *Phys. Rev. B* **95**, 064307. (doi:10.1103/PhysRevB.95.064307)
18. Silverberg JL, Evans AA, McLeod L, Hayward RC, Hull T, Santangelo CD, Cohen I. 2014 Using origami design principles to fold reprogrammable mechanical metamaterials. *Science* **345**, 647–650. (doi:10.1126/science.1252876)
19. Fang H, Chu S-CA, Xia Y, Wang KW. 2018 Programmable self-locking origami mechanical metamaterials. *Adv. Mater.* **30**, 1706311. (doi:10.1002/adma.201706311)
20. Dudte LH, Vouga E, Tachi T, Mahadevan L. 2016 Programming curvature using origami tessellations. *Nat. Mater.* **15**, 583–588. (doi:10.1038/NMAT4540)
21. Saito K, Tsukahara A, Okabe Y. 2016 Designing of self-deploying origami structures using geometrically misaligned crease patterns. *Proc. R. Soc. A* **472**, 20150235. (doi:10.1098/rspa.2015.0235)
22. Boatti E, Vasios N, Bertoldi K. 2017 Origami metamaterials for tunable thermal expansion. *Adv. Mater.* **29**, 1700360. (doi:10.1002/adma.201700360)
23. Wang Z, Jing L, Yao K, Yang Y, Zheng B, Soukoulis CM, Chen H, Liu Y. 2017 Origami-based reconfigurable metamaterials for tunable chirality. *Adv. Mater.* **29**, 1700412. (doi:10.1002/adma.201700412)
24. Zhou X, Zang S, You Z. 2016 Origami mechanical metamaterials based on the Miura-derivative fold patterns. *Proc. R. Soc. A* **472**, 20160361. (doi:10.1098/rspa.2016.0361)

25. Bhovad P, Kaufmann J, Li S. 2019 Peristaltic locomotion without digital controllers: Exploiting multi-stability in origami to coordinate robotic motion. *Extreme Mech. Lett.* **32**, 100552. (doi:10.1016/j.eml.2019.100552)
26. Overvelde JTB, Weaver JC, Hoberman C, Bertoldi K. 2017 Rational design of reconfigurable prismatic architected materials. *Nature* **541**, 347–352. (doi:10.1038/nature20824)
27. Faber JA, Arrieta AF, Studart AR. 2018 Bioinspired spring origami. *Science* **359**, 1386–1391. (doi:10.1126/science.aap7753)
28. Baranger E, Guidault PA, Cluzel C. 2011 Numerical modeling of the geometrical defects of an origami-like sandwich core. *Compos. Struct.* **93**, 2504–2510. (doi:10.1016/j.compstruct.2011.04.011)
29. Jianguo C, Xiaowei D, Yuting Z, Jian F, Ya Z. 2016 Folding behavior of a foldable prismatic mast with Kresling origami pattern. *J. Mech. Robot.* **8**, 031004. (doi:10.1115/1.4032098)
30. Wang B, Zhou C. 2017 The imperfection-sensitivity of origami crash boxes. *Int. J. Mech. Sci.* **121**, 58–66. (doi:10.1016/j.ijmecsci.2016.11.027)
31. Fang H, Li S, Wang KW. 2016 Self-locking degree-4 vertex origami structures. *Proc. R. Soc. A* **472**, 20160682. (doi:10.1098/rspa.2016.0682)
32. Ma J, Song J, Chen Y. 2018 An origami-inspired structure with graded stiffness. *Int. J. Mech. Sci.* **136**, 134–142. (doi:10.1016/j.ijmecsci.2017.12.026)
33. Grenestedt JL. 1998 Influence of wavy imperfections in cell walls on elastic stiffness of cellular solids. *J. Mech. Phys. Solids* **46**, 29–50. (doi:10.1016/S0022-5096(97)00035-5)
34. Symons DD, Fleck NA. 2008 The imperfection sensitivity of isotropic two-dimensional elastic lattices. *J. Appl. Mech.* **75**, 051011. (doi:10.1115/1.2913044)
35. Liu L, Kamm P, García-Moreno F, Banhart J, Pasini D. 2017 Elastic and failure response of imperfect three-dimensional metallic lattices: the role of geometric defects induced by Selective Laser Melting. *J. Mech. Phys. Solids* **107**, 160–184. (doi:10.1016/j.jmps.2017.07.003)
36. Liu K, Paulino GH. 2017 Nonlinear mechanics of non-rigid origami: an efficient computational approach. *Proc. R. Soc. A* **473**, 20170348. (doi:10.1098/rspa.2017.0348)
37. Filipov ET, Liu K, Tachi T, Schenk M, Paulino GH. 2017 Bar and hinge models for scalable analysis of origami. *Int. J. Solids Struct.* **124**, 26–45. (doi:10.1016/j.ijsolstr.2017.05.028)
38. Xu H, Gardoni P. 2018 Improved latent space approach for modelling non-stationary spatial–temporal random fields. *Spatial Statistics* **23**, 160–181. (doi:10.1016/j.spasta.2018.01.003)
39. Vanmarcke E. 1983 *Random fields: analysis and synthesis*. Cambridge, MA: MIT Press.
40. Lang RJ. 2018 *Twists, tilings, and tessellations*. Boca Raton, FL: CRC Press.
41. Ajdari A, Nayeb-Hashe mi H, Vaziri A. 2011 Dynamic crushing and energy absorption of regular, irregular and functionally graded cellular structures. *Int. J. Solids Struct.* **48**, 506–516. (doi:10.1016/j.ijsolstr.2010.10.018)
42. Ma J, Hou D, Chen Y, You Z. 2016 Quasi-static axial crushing of thin-walled tubes with a kite-shape rigid origami pattern: numerical simulation. *Thin-Walled Struct.* **100**, 38–47. (doi:10.1016/j.tws.2015.11.023)
43. Rogers J, Huang Y, Schmidt OG, Gracias DH. 2016 Origami MEMS and NEMS. *MRS Bull.* **41**, 123–129. (doi:10.1557/mrs.2016.2)
44. Leon SE, Paulino GH, Pereira A, Menezes IFM, Lages EN. 2011 A unified library of nonlinear solution schemes. *Appl. Mech. Rev.* **64**, 040803. (doi:10.1115/1.4006992)
45. Ogden RW. 1997 *Non-linear elastic deformations*. New York, NY: Dover Publications.